Electronic supplementary information for

Centrifugal microfluidic system for colorimetric sample-to-answer detection of viral pathogens

Matthias Geissler,[a] Daniel Brassard,[a] Nadine Adam,[b] Neda Nasheri,[b,c] Ana Victoria C. Pilar,[b] Kyle Tapp,[b] Liviu Clime,[a] Caroline Miville-Godin,[a] Maxence Mounier,[a] Christina Nassif,[a] Ljuboje Lukic,[a] Lidija Malic,[a] Nathalie Corneau,[b] and Teodor Veres[a]

[a] *Life Sciences Division, National Research Council of Canada, 75 de Mortagne Boulevard, Boucherville, QC, J4B 6Y4, Canada*

[b] *Bureau of Microbial Hazards, Health Canada, 251 Sir Frederick Banting Driveway, Ottawa, ON, K1A 0K9, Canada*

[c] *Department of Biochemistry, Microbiology and Immunology, Faculty of Medicine, University of Ottawa, 451 Smyth Road, Ottawa, ON, K1H 8M5, Canada*

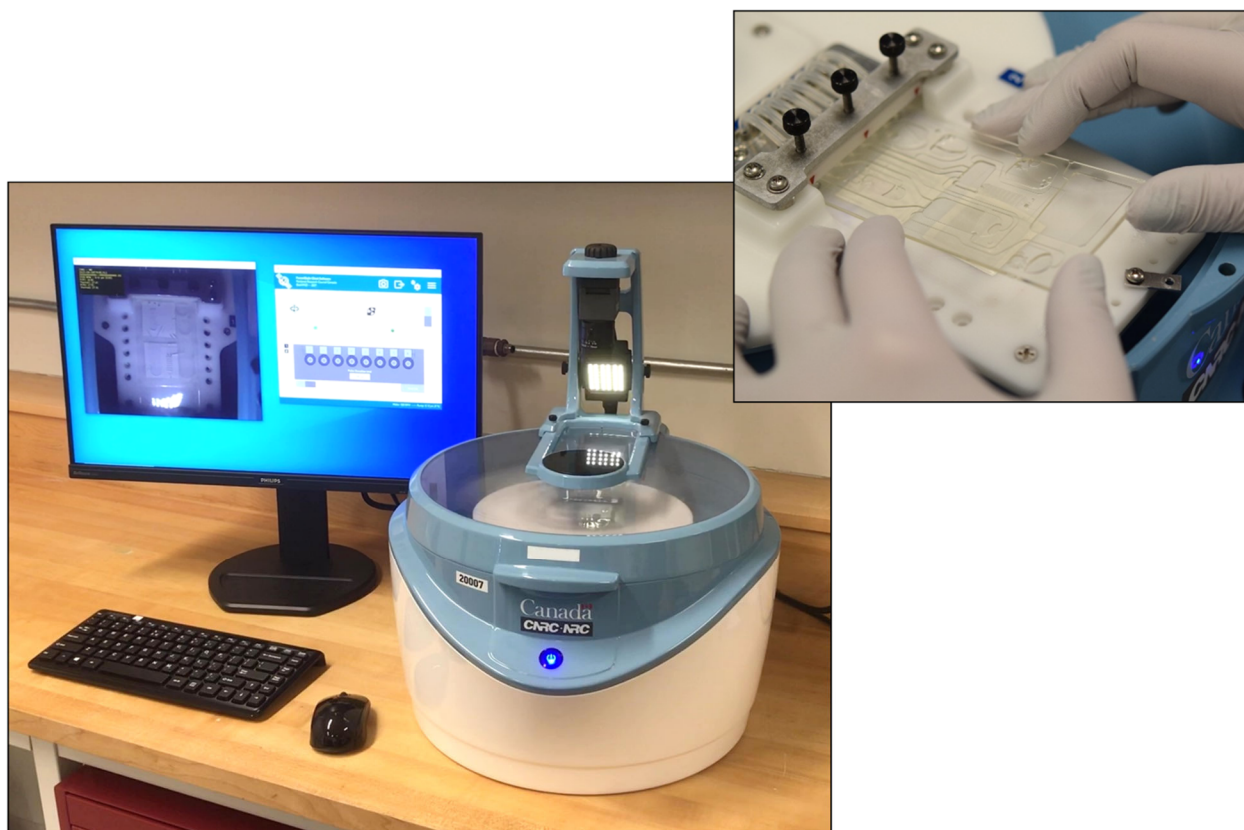# Contents

1 Centrifugal microfluidic platform

Fig. S1   Centrifugal microfluidic platform used within this work. The rotating stage is equipped with a pneumatic pumping and pressure control system to mediate fluid displacement during rotation. The cartridge (filled with buffers and reagents for sample-to-answer virus detection) is aligned with a movable manifold lid on the rotating stage. The pneumatic system is conceived for applying pressure in the range of -5 to $+10$ psi. Non-pressurized ports serve as vent and allow air to be released from the cartridge. Thermoelectric elements on the rotating stage are covered with thermal tape to ensure efficient heat transfer from the to the cartridge during lysis and PCR amplification steps. A LabVIEW interface allows for automating the assay *via* scripts that can be customized according to the requirements of the protocol.

2 Microfluidic cartridge

Table S1 Reservoirs on the microfluidic cartridge

Chamber	Purpose	Assay component	Input volume (μL)	Port used for filling
A	Lysis chamber	Sample	30	Sample port S
B	PCR chamber	PCR master mix	20 (or 30)	Pressure port 4
C	Storage reservoir	HS	40	Pressure port 1
D	Transfer chamber	–	–	–
E	Waste reservoir	–	–	–
F	Storage reservoir	HRP-conjugated Ab	50	Pressure port 6
G	Storage reservoir	TMB	50	Pressure port 7
H	Storage reservoir	PBST wash buffer	130	Pressure port 8

3 Sedimentation of particles

We tested the compatibility of the microfluidic design to purify viral lysate from superparamagnetic particles using Dynabeads M-270 that are 2.8 μm in diameter (Fig. S2a). We have previously demonstrated the efficacy of these particles for the extraction of viral pathogens from food samples.[1,2] Observation of the sedimentation process reveals that beads accumulate at the bottom of the lysis chamber while the liquid is clearing gradually during rotation (Fig. S2b and S2c). Inspection of the supernatant recovered from the cartridge (Fig. S2d and S2e) suggests a removal rate of >99.98% when rotating at 800 rpm for 15 min—a condition that allows for producing purified, PCR-compatible lysate without the need for implementing a magnetic capture format on the platform.[3]
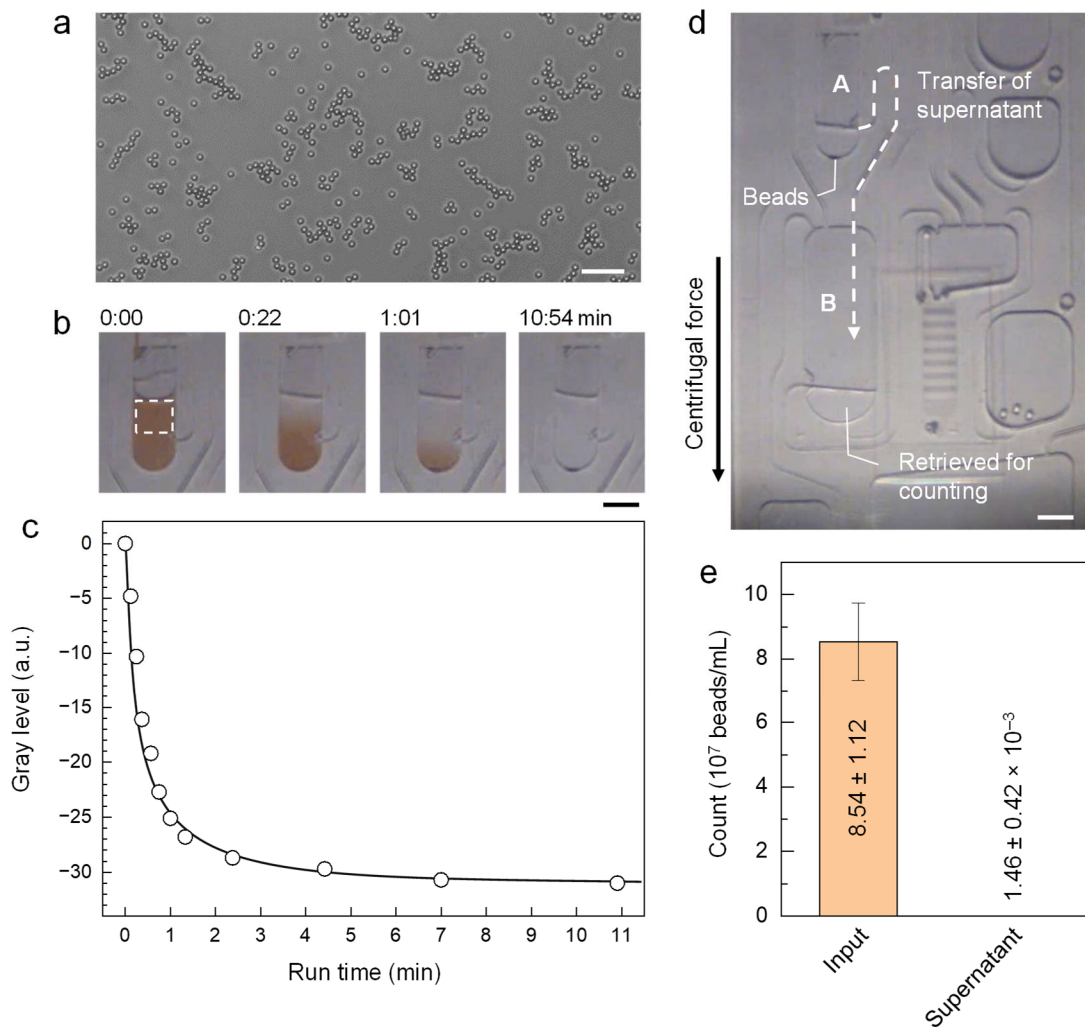
Fig. S2 Validation of on-chip sedimentation using Dynabeads M-270. (a) Optical microscopy image of the input sample, obtained by dilution of the original suspension in PBST. Scale bar: 20 µm. (b) Stroboscopic images of the lysis chamber (A) at different time intervals while the platform is rotating at 800 rpm. Scale bar: 5 mm. (c) Evolution of the sedimentation process. Changes in gray levels were determined above the intersection with the transfer channel as indicated by the window outlined in (b). The line in the graph serves as a guide to the eye. (d) Stroboscopic image of the cartridge upon transferring 20 µL of supernatant to the PCR chamber (B). Centrifugation was maintained at 800 rpm for 15 min. The purified fraction was retrieved once the platform was brought to a stand-still. Scale bar: 5 mm. (e) Plot showing the number of beads counted for input sample and supernatant (see Experimental section for details). On-chip purification was conducted in duplicate using two different cartridges ($n = 2$).
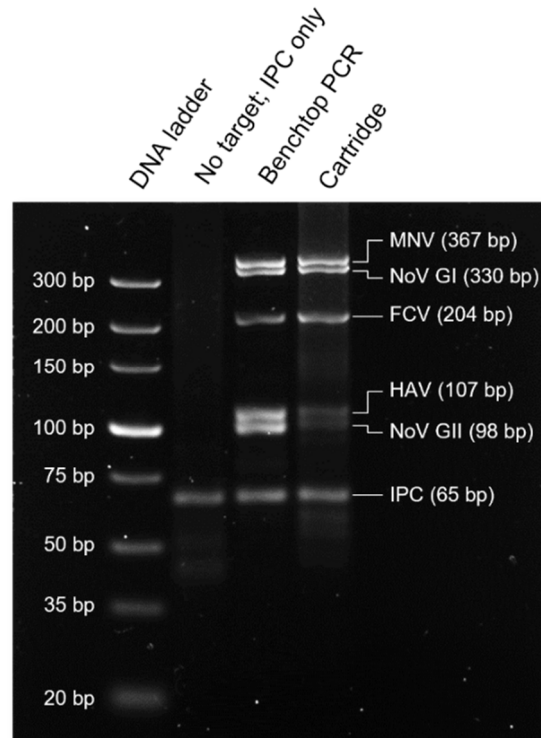
4 Gel images

Fig. S3 Fluorescence gel image showing similar band patterns of gene targets produced on-chip and by using a benchtop PCR instrument. Multiplex RT-PCR amplification of viral RNA from all five target viruses and IPC DNA results in six distinct amplicon bands. When no template is added, only IPC is amplified (as demonstrated using benchtop PCR).
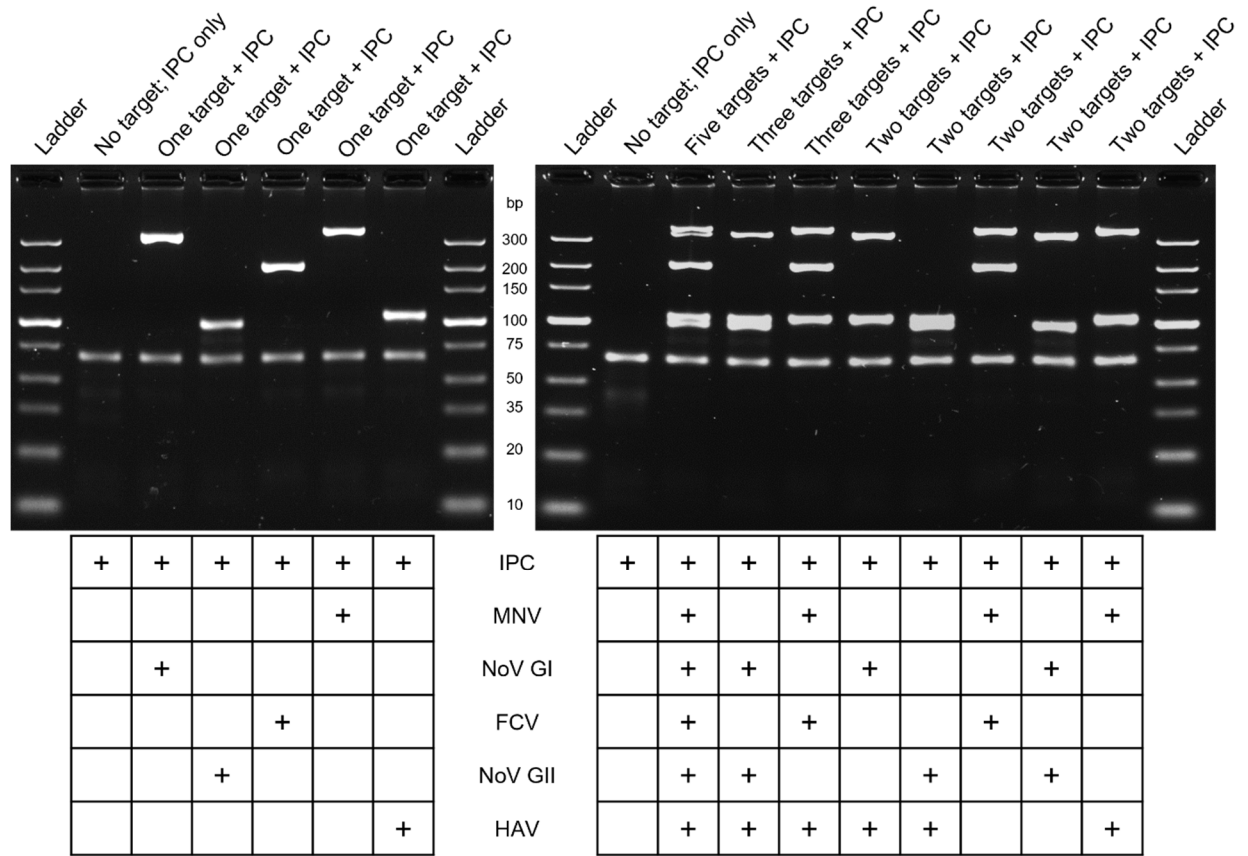
Fig. S4 Gel images of selected viral amplicons produced using the multiplex RT-PCR assay developed in this work. Amplification was performed off-chip using a benchtop PCR instrument (see Experimental section for details).

5 Numerical simulations

We performed finite element numerical simulations to investigate the influence of cartridge design parameters and centrifugal force field on assay performance using Brinkman's equation[4] related to flow in porous media

$$\frac{\eta}{\kappa}\vec{u} = \nabla \cdot \left[-p\boldsymbol{I} + \frac{\eta}{\varepsilon_p}(\nabla\vec{u} + (\nabla\vec{u})^T) \right] + \vec{f} \tag{1}$$

where η is the dynamic viscosity of the liquid, κ is the permeability of the porous medium, ε is the porosity, p is the applied pressure, $\boldsymbol{I}$ is the identity matrix, $\vec{u}$ is the liquid velocity field with $\nabla \cdot \vec{u} = 0$ (i.e., incompressible fluid). The body force vector field $\vec{f}$ is expressed as

$$\vec{f}(\vec{r}) = -\rho\vec{\omega} \times (\vec{\omega} \times \vec{r}) - 2\rho\vec{\omega} \times \vec{u} \tag{2}$$

where ρ is the mass density of the liquid, $\vec{\omega}$ is the angular velocity, and $\vec{r}$ is the absolute value of the radial position vector with respect to the rotation center, to account for contributions from the centrifugal field $\vec{f}_{cf} = -\rho\vec{\omega} \times (\vec{\omega} \times \vec{r})$ acting on the radial direction and from the Coriolis force $\vec{f}_{Coriolis} = -2\rho\vec{\omega} \times \vec{u}$ acting on the circumferential direction.

The microfluidic chamber was translated into a 2D computational domain (Fig. S5a) consisting of 71 000 mesh elements (Fig. S5b). Regions outside arrays are characterized by high porosity ($\varepsilon_0 = 1$) and high permeability ($\kappa_0 = h^2/16$)[5] while regions inside arrays are defined as $\varepsilon_p < \varepsilon_0$ and $\kappa_p < \kappa_0$ due to the presence of pillars. An absolute value of $\varepsilon_p = 0.841$ was derived from the fill factor of the micropillar array, (e.g., 0.159 for a diagonal square lattice with d = 18 μm and a = 40 μm). To determine κ_p, we relied on recent work by Chakrapani *et al.*[6] which allows for estimating permeability of a Newtonian flow through a

diagonal square lattice of pillars (confined between top and bottom plates, respectively) as $\kappa_p = 1.6 \times 10^{-10}$ m^2 = $0.178\,\kappa_0$. No-slip boundary conditions were imposed on all boundaries except for inlet and outlet where $p = 0$ and a constant flow rate of $Q = 50$ μL/min are applied.
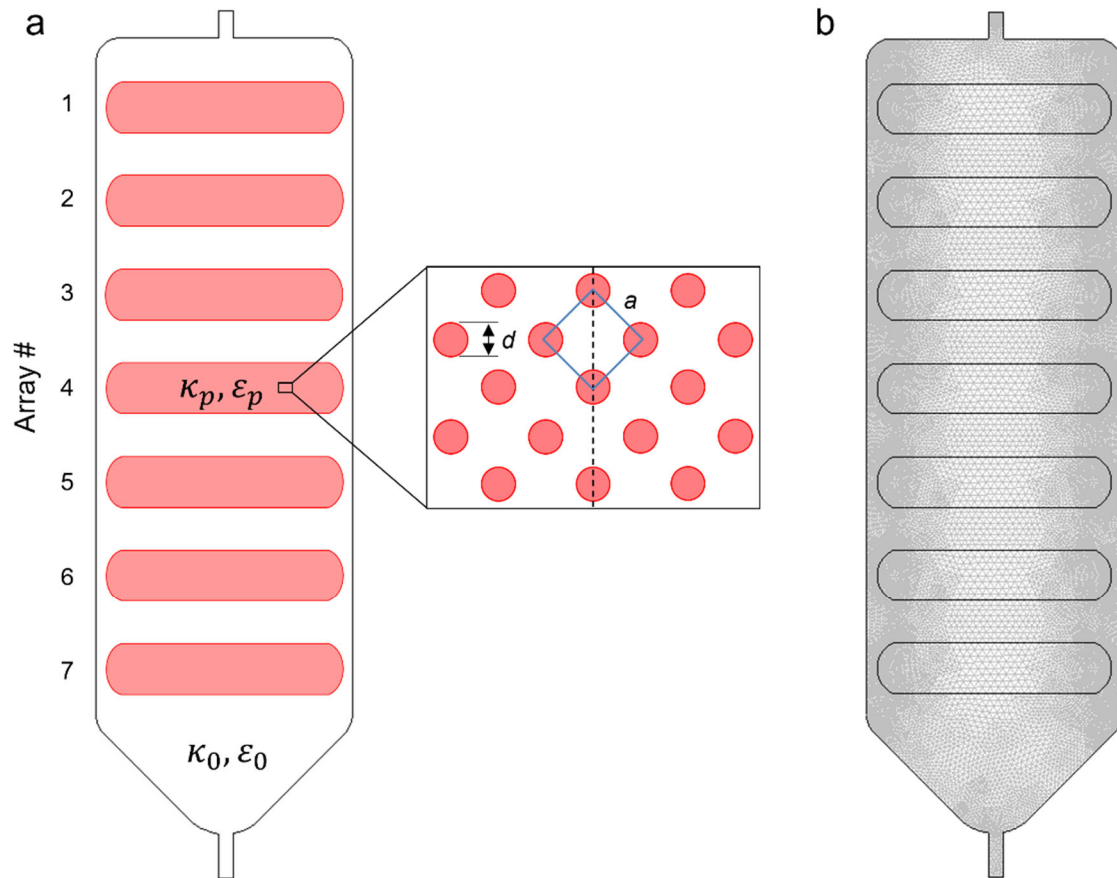

Fig. S5 2D Computational domain used for numerical simulation. (a) Design of the microfluidic chamber (top view) as regions with distinct porosity and permeability. Micropillars within each array are arranged as a diagonal square lattice (d = 18 μm, a = 40 μm). (b) Size and distribution of the mesh elements that constitute the computational domain.
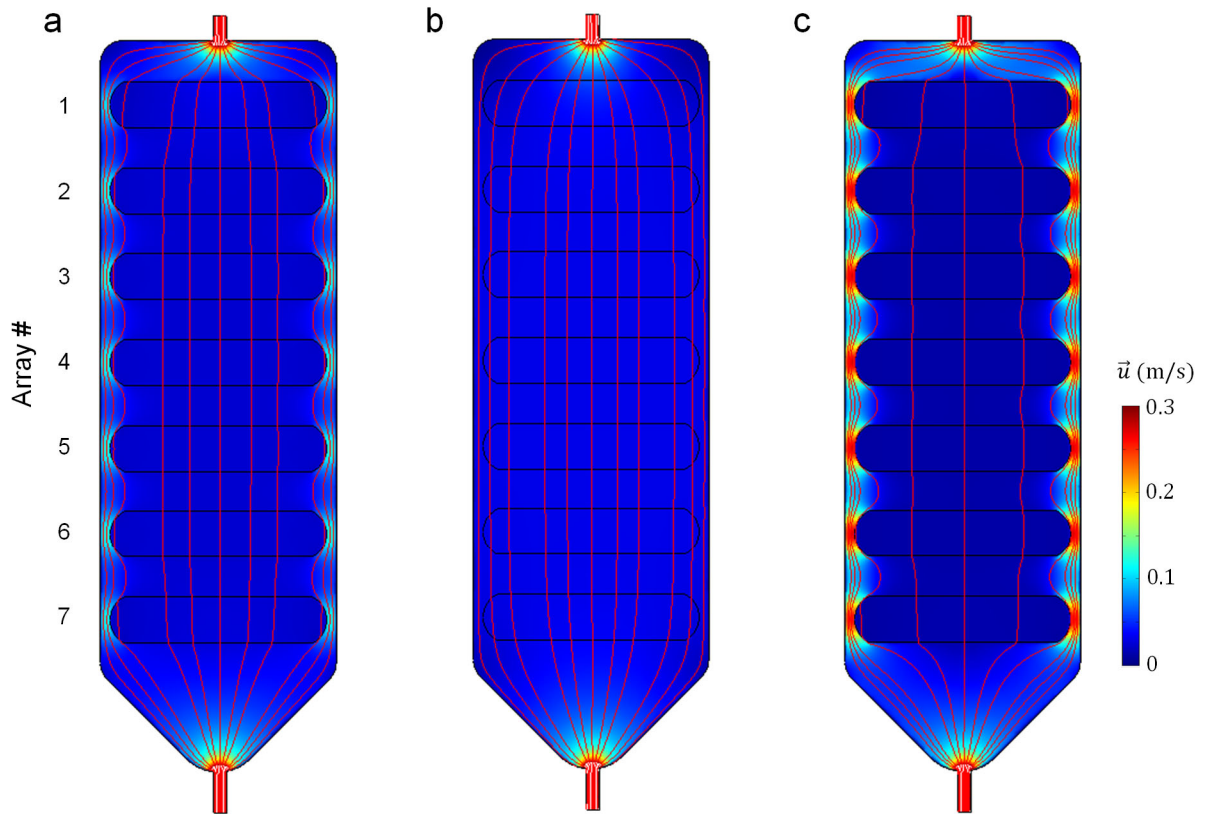
Fig. S6 Simulated flow across micropillar arrays with different configurations. Contour fill plots showing the velocity field and stream lines for (a) $\varepsilon_p = 0.841$ and $\kappa_p = 0.178\,\kappa_0$; (b) $\varepsilon_p = 1$ and $\kappa_p = \kappa_0$ (that is, an empty array with no pillars); and (c) $\varepsilon_p = 0.841$ and $\kappa_p = 0.04\,\kappa_0$. In all cases, a flow rate of $Q = 50$ µL/min was applied to inlet and outlet, respectively. The frequency of rotation was set to $f = 13.33$ Hz (clock-wise direction). The direction of flow is from top to bottom.
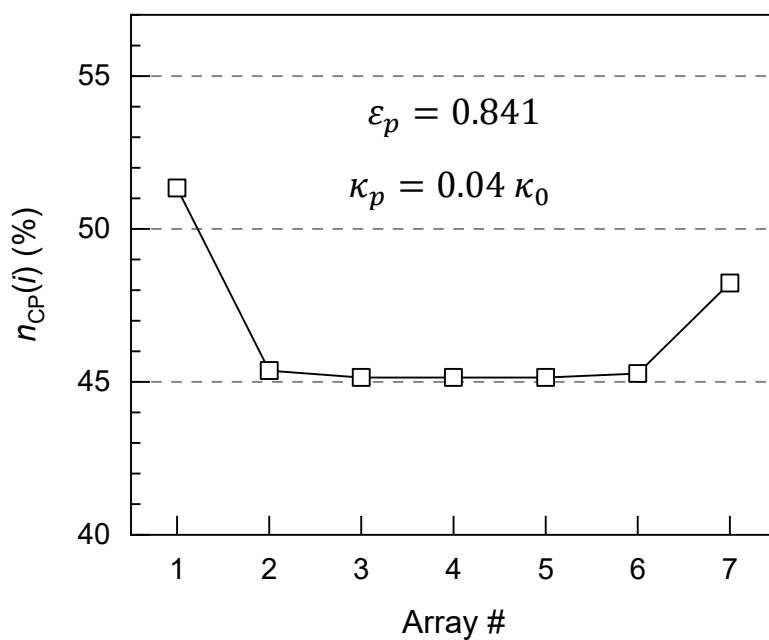
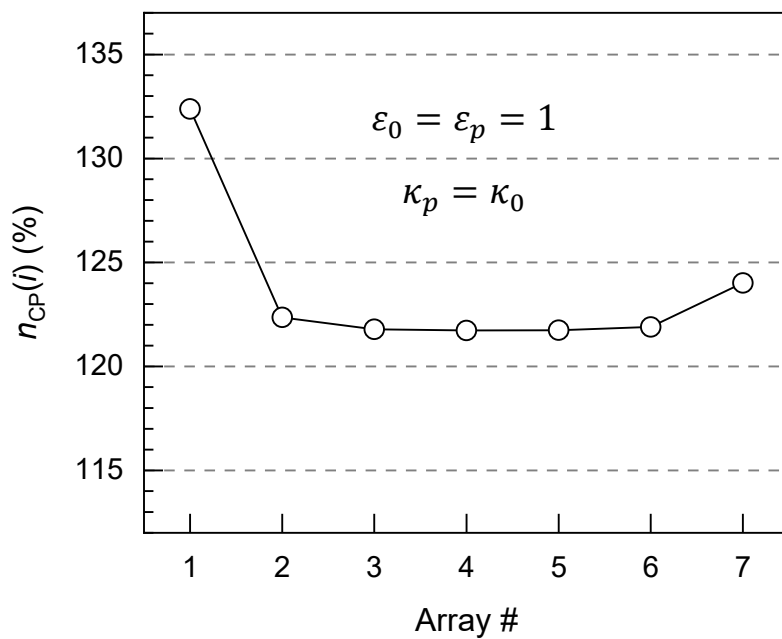**Fig. S7** Plots of the number of color pigments for micropillar arrays with two different parameter sets used for the simulation.

We define $N_{CP}(i)$ as the total number of color pigments attached to the pillars in each of the seven arrays, $i = \overline{1,7}$. For any given micropillar, the total amount of color pigments developed on its surface is proportional to the volume of liquid that has passed that pillar, and therefore to the velocity of the stream lines surrounding it. $N_{CP}(i)$ is then obtained by summing up the contributions for all pillars with the array. In the numerical simulation, this is equivalent to integrating the velocity field $|\vec{u}|$ over the entire area of the array, Ω_i, $i = \overline{1,7}$.

$$N_{CP}(i) \propto \iint_{\Omega_i} |\vec{u}|\, dS$$

This approximation is valid only if the reaction and adsorption rates of the species at the surface do not depend on the local velocity of the fluid flow. We also assume that assay components are not depleted during their passage across the microarray.

For the purpose of comparison, we plot in Fig. 5c as well as in Fig. S7 a normalized quantity $n_{CP}(i)$ corresponding to

$$n_{CP}(i) = \frac{N_{CP}(i)}{N_{CP+}}$$

where N_{CP+} is the maximum value of coloration obtained for a positive signal.

Table S2 Solver parameters

Parameter	Value
Degrees of freedom	321 000
Number of tetrahedral elements	71 000
Solver	Stationary → Autoselect solver
Relative tolerance	10^{-6}
Maximum number of iterations	25
Linear system solver	Direct (SPOOLES)

6 Use of non-isolated micropillar arrays

We produced non-isolated micropillar arrays where the structured segments span the entire width of the chamber (Fig. S8a and S8b). The implementation of a physical gap into the design isolates the array and so makes it possible to pin the probe liquid at the edge of the structured area during spotting.[7,8] Elimination of the gap, in turn, yields a non-isolated array which is no longer able to effectively halt the wicking front (Fig. S8c). As a result, we observed color formation in areas that were intentionally left empty during spotting (Fig. S8d)—a finding that constitutes an impediment to the use of these templates for analytical testing.
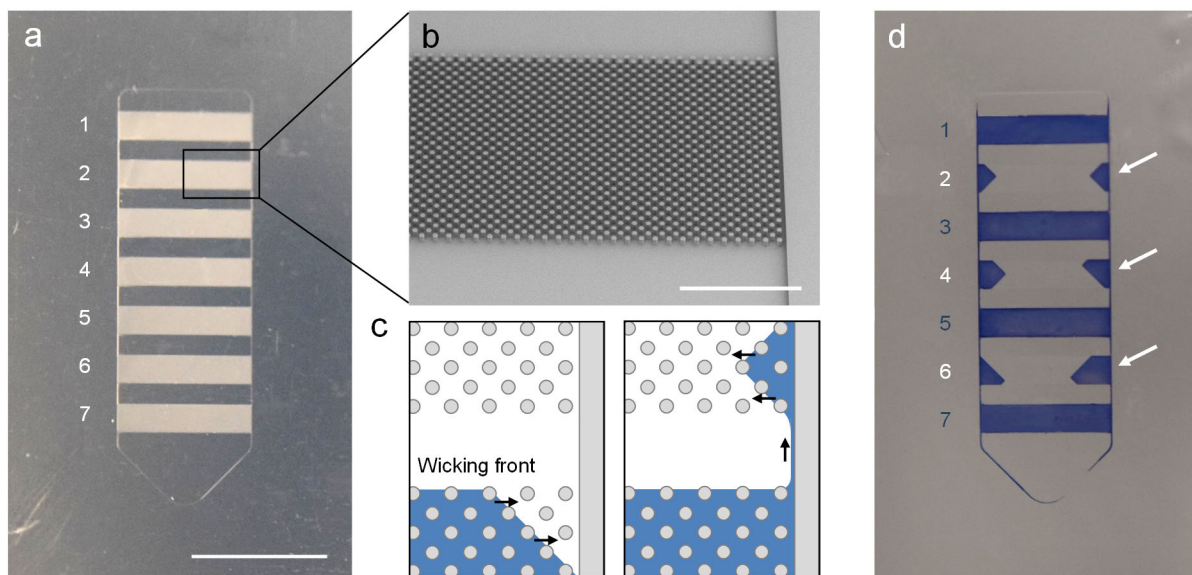
Fig. S8 Use of non-isolated micropillar arrays. (a) Photograph showing the configuration of the template (top view). The substrate was produced in Zeonor using hot embossing. Scale bar: 5 mm. (b) SEM image showing the structure of the array at the intersection with the chamber wall. Scale bar: 500 µm. (c) Scheme depicting the propagation of probe liquid within the template during spotting. The wicking front can easily be drawn outside the array, causing liquid to spill over into neighboring arrays. (d) Photograph of a non-isolated micropillar array substrate used in a colorimetric assay. Arrays with odd numbers were spotted with IPC probe; arrays with even numbers were intentionally left empty. The presence of blue colored dye in the outer portions of the non-spotted arrays is indicative of the difficulty to confine probe solution. Assay steps were conducted off-chip using passive incubation.

7 References

1 M. Suresh, J. Harlow and N. Nasheri, *Food Microbiol.*, 2019, **84**, 103254.

2 N. Nasheri, J. Harlow, A. Chen, N. Corneau and S. Bidawid, *J. Food Prot.*, 2020, **83**, 388–396.

3 L. Malic, D. Brassard, D. Da Fonte, C. Nassif, M. Mounier, A. Ponton, M. Geissler, M. Shiu, K. J. Morton and T. Veres, *Lab Chip*, 2022, **22**, 3157–3171.

4 H. C. Brinkman, *Appl. Sci. Res.*, 1947, **A1**, 27–34.

5 H. Bruus, *Theoretical Microfluidics*, Oxford University Press, New York, NY, 2007, p. 75.

6 T. H. Chakrapani, H. Bazyar, R. G. H. Lammertink, S. Luding and W. K. den Otter, *Soft Matter*, 2023, **19**, 436–450.

7 C. Semprebon, P. Forsberg, C. Priest and M. Brinkmann, *Soft Matter*, 2014, **10**, 5739–5748.

8 M. Geissler, L. Malic, K. J. Morton, L. Clime, J. Daoud, J. A. Hernández-Castro, N. Corneau, B. W. Blais and T. Veres, *Anal. Chem.*, 2020, **92**, 7738–7745.